Journal of
Materials Chemistry A

PAPER

View Article Online
View Journal

Cite this: DOI: 10.1039/c7ta02640d

Defect accumulation in swift heavy ion-irradiated CeO_2 and ThO_2†

Raul I. Palomares,[a] Jacob Shamblin,[ab] Cameron L. Tracy,[c] Joerg Neuefeind,[d] Rodney C. Ewing,[c] Christina Trautmann[ef] and Maik Lang*[a]

Received 26th March 2017
Accepted 21st May 2017

DOI: 10.1039/c7ta02640d

rsc.li/materials-a

Neutron total scattering was used to investigate defect accumulation mechanisms in CeO_2 and ThO_2 irradiated with 2.2 GeV Au ions. Pair distribution function (PDF) analysis was applied to characterize the local structural evolution and irradiation-induced defects as a function of irradiation fluence. CeO_2 exhibits a greater amount of disorder than ThO_2 under the same irradiation conditions. The local structures of the two materials evolve differently as a function of ion fluence, even if similar defects are produced. The PDF analysis indicates that oxygen dimer and/or peroxide defects with $\langle O–O \rangle$ distances of ~1.45 Å are formed in CeO_2, while irradiation-induced defects in ThO_2 result in a change in the mean O–Th–O bond angle and a distortion of local ThO_8 polyhedra. Understanding how bound oxygen defects, such as peroxide, affect bulk oxygen transport in CeO_2 will aid in better predicting and improving properties of fluorite structure materials for fast ion conductor applications.

1. Introduction

Fluorite-structure oxides, such as CeO_2 and ThO_2, exhibit excellent structural stability under a wide range of temperatures and chemical environments, making them attractive candidates for an array of engineering applications, including industrial catalysts,[1,2] oxygen sensors,[3] nuclear fuels,[4–6] and solid oxide fuel cell (SOFC) electrolytes.[7,8] The resilience of fluorite-type oxides for several of these applications is largely attributed to the relatively open structure that can accommodate high concentrations of defects. Consequently, numerous investigations have focused on improving physical and chemical properties by exploiting the formation and distribution of defects in the fluorite defect-structure. For example, the strategic incorporation of defects in CeO_2 can lead to increased oxygen conductivity, allowing for lower operating temperatures in advanced SOFCs.[9] Improved oxygen ion mobility is typically achieved through doping[9–11] or the manipulation of grain boundaries[12] and strain.[13] However, several investigations suggest that ionic conductivity can also be enhanced *via* the use of external perturbations, such as high-energy irradiation with swift heavy ions.[14–16]

Swift heavy-ion irradiation is a valuable tool for manipulating the structure of materials at the nanoscale. During irradiation, these ions of specific energy of ~1 MeV u^{-1} or above deposit substantial quantities of energy to the electronic system of the target material over sub-picosecond timescales. This results in electronic excitation and ionization processes, which modify interatomic forces and lead to permanent atomic displacement when the relaxation from the perturbed state is sufficiently rapid, and recovery kinetics are sufficiently slow as to preclude recovery to the initial structure.[17] The primary result of swift heavy ion irradiation is the formation of spatially-confined, cylindrical damage zones of a few nanometers in diameter, called ion tracks, along the linear trajectory of the ions.[18] Depending on the specific material and on the generation, recovery and distribution of defects, the ion track region can undergo a variety of modifications, such as densification,[19] phase transformations,[20] or amorphization.[21] In CeO_2, ion tracks have lower atomic density than the surrounding bulk and exhibit high concentrations of oxygen vacancies and small vacancy clusters.[22] Thus, disordering of the anion sublattice (*i.e.*, the incorporation of oxygen vacancies) using ion beams may be used to enhance the oxygen conductivity of undoped CeO_2 and ThO_2, which otherwise do not exhibit particularly high levels of oxygen conductivity.

A major challenge in understanding and predicting irradiation-induced modifications in these binary oxides, however, lies in probing the anion sublattice in the presence of high Z cations. Oxygen ions in CeO_2 and ThO_2 outnumber

---

[a] *Department of Nuclear Engineering, University of Tennessee, Knoxville, Tennessee 37996, USA. E-mail: mlang2@utk.edu*

[b] *Department of Physics and Astronomy, University of Tennessee, Knoxville, Tennessee 37996, USA*

[c] *Department of Geological Sciences, Stanford University, Stanford, California 94305, USA*

[d] *Chemical and Engineering Materials Division, Spallation Neutron Source, Oak Ridge National Laboratory, Oak Ridge, Tennessee 37831, USA*

[e] *GSI Helmholtzzentrum für Schwerionenforschung, 64291 Darmstadt, Germany*

[f] *Technische Universität Darmstadt, 64287 Darmstadt, Germany*

† Electronic supplementary information (ESI) available. See DOI: 10.1039/c7ta02640d

cations 2 : 1, yet the high *Z*-contrast between oxygen and the cations renders oxygen atoms nearly invisible by conventional X-ray or electron scattering techniques. For example, small-angle X-ray scattering (SAXS), which is uniquely capable of detecting the dimensions of ion tracks,[19] is insensitive to density fluctuations specific to the anion sublattice, such that it is not useful for characterizing oxygen-deficient ion tracks in CeO_2. This is due to the strong X-ray scattering by cerium atoms, relative to that of oxygen atoms ($Z_{Ce} = 58$ *vs.* $Z_O = 8$). High resolution transmission electron microscopy (TEM) and Raman spectroscopy are valuable alternatives; however, these techniques are spatially limited to areas of interest (TEM) or yield data that are difficult to interpret quantitatively (Raman). Neutron total scattering provides a unique means of analyzing bulk-averaged information from both the Bragg- and diffuse-scattering components by simultaneously probing the long- and short-range structure of a given material. Using neutrons, the scattering is only weakly proportional to *Z* and the cation-to-anion coherent scattering ratios are improved to approximately 0.83 and 1.78 for CeO_2 and ThO_2, respectively. This means that the cation and anion sublattices can be probed simultaneously, and modifications to each subsystem can be distinguished.

Neutron scattering has rarely been applied to the study of ion irradiation-induced defects, primarily due to the challenge of obtaining sufficiently large irradiated sample volumes. Neutron scattering experiments typically require large sample masses (>1 g) owing to the relatively weak intensity of neutron sources as compared to with X-ray sources. In addition, ion beams typically have short penetration depths in irradiated materials (several nm to µm), even when using ions with hundreds of MeV of kinetic energy. In this study, a unique ion irradiation scheme was employed in order to investigate the defect accumulation mechanisms in swift heavy ion irradiated CeO_2 and ThO_2. The irradiated samples were characterized using neutron total scattering measurements that were collected as a function of irradiation fluence. The pair distribution function analysis reveals the presence of small oxygen defects and distorted ThO_8 polyhedra in CeO_2 and ThO_2, respectively. These results provide valuable insight, not only for the continued development of fluorite structure SOFC electrolytes, but also for elucidating the structural behavior and evolution of CeO_2 inert matrix fuels and ThO_2 nuclear fuel concepts under fission-fragment-like irradiation.[4–6,23,24]

2. Experimental

2.1 Ion irradiation

Special sample holders were designed to homogenously irradiate sufficient sample powder (∼100 mg) for neutron total scattering measurements. In order to avoid ions stopping in the material and to yield near-constant energy loss within the samples, the surface area exposed to the beam was maximized and the sample thickness was minimized. The maximum sample thickness required to ensure full penetration of ions was determined using energy loss calculations. The calculations were performed with the SRIM-2008 code[25] and the density correction factor from Lang *et al.*[26] The sample densities were assumed to be 60% theoretical density because this value represents the maximum sample density achieved from cold, uniaxial compression under similar loads.[27] The ion ranges calculated based on these assumptions are 91 µm and 89 µm for polycrystalline CeO_2 and ThO_2, respectively. Therefore, the samples prepared for ion irradiation were made approximately 75 µm thick.

The CeO_2 and ThO_2 samples were prepared with microcrystalline powders obtained from Alfa Aesar (99.9% purity) and IBILabs (99.99% purity), respectively. The powders were uniaxially pressed into 1 cm diameter, 75 µm-deep circular indentations that were machined into small aluminum plates (Fig. 1). The filled aluminum holders were tightly wrapped with 10 µm-thick aluminum foil for secure handling and subsequent shipping. Nine sample holders of each compound were affixed to a 5 cm × 5 cm aluminum plate and simultaneously irradiated to the desired ion fluences (5×10^{11}, 1×10^{12}, and 5×10^{12} ions per cm^2). The irradiation was performed at room temperature and under vacuum at the X0 beamline of the Universal Linear Accelerator (UNILAC) at the GSI Helmholtz Center for Heavy Ion Research in Darmstadt, Germany with a defocused beam of ^{197}Au ions with initial kinetic energy of 2.2 GeV. The kinetic energy was approximately 2 GeV at the sample surface after the ions passed through the Al foil. The energy loss in this specific energy regime is primarily electronic with negligible nuclear energy loss (ESI Fig. 1†). The linear electronic energy loss calculated using the SRIM code and averaged over the entire sample thickness is 41.3 ± 6.6 keV nm^{-1} for CeO_2 and 41.9 ± 7.1 keV nm^{-1} for ThO_2. The uncertainty values represent the upper and lower bounds to the linear energy loss over the sample thickness.

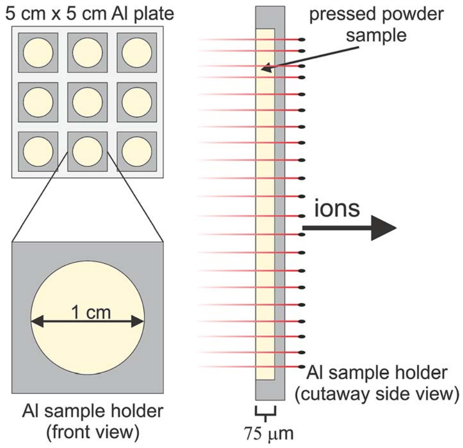

Fig. 1 Schematic of the sample holders for ion irradiation. Powders of CeO_2 and ThO_2 (yellow) were uniaxially pressed into 75 µm deep, 1 cm diameter cylindrical indentations that were machined into thin aluminum plates (grey). Nine sample holders were fixed on a 5 cm × 5 cm aluminum plate for ion irradiation (top left). The cutaway side view (right) shows the orientation of the holder during ion irradiation.

2.2 Neutron total scattering

Irradiation-induced disorder in the CeO_2 and ThO_2 samples were characterized by neutron total scattering measurements. After irradiation, the samples were removed from the aluminum sample holders with a blunt-tipped needle and loaded into thin-walled quartz tubes (0.01 mm and 0.38 mm wall thickness for CeO_2 and ThO_2 samples, respectively). Neutron scattering data were collected at room temperature at the Nanoscale-Ordered MAterials Diffractometer (NOMAD) beamline[28] at the Spallation Neutron Source (SNS) at Oak Ridge National Laboratory. The collection time for each sample was 60 minutes.

The neutron scattering data were analyzed by structural refinement of both diffraction patterns and pair distribution functions (PDFs). The NOMAD detectors were calibrated using scattering from diamond powder, and silicon powder was used to derive the instrument parameters required for Rietveld refinement. Rietveld refinement of diffractograms was performed using GSAS.[29] The diffractograms were fit using the fluorite structure model ($Fm\bar{3}m$) with the cations and anions occupying the 4*a* and 8*c* Wyckoff sites, respectively (ESI Fig. 2†). In total, seven parameters were used for Rietveld refinement: the scale factor, isometric unit cell parameter ($a = b = c$), atomic displacement parameters (ADPs), site occupancies, and the zero point. The ADPs were, according to symmetry constraints, isotropic, *i.e.*, $U_{11} = U_{22} = U_{33}$ and $U_{12} = U_{23} = U_{13} = 0$, and one ADP parameter was assigned to each Wyckoff site. The diffraction patterns from three detector banks (66°, 122°, and 154° scattering angles) were fit simultaneously for each sample during Rietveld refinement.

In order to obtain the structure factor, $S(Q)$, the scattering intensity was normalized to the scattering from a solid vanadium rod and the background was subtracted using an empty quartz tube with the same wall thickness as the sample tube. The PDF, $G(r)$, was calculated by the Fourier transform of $S(Q)$ with $Q_{\min} = 0.1\ \text{Å}^{-1}$ and $Q_{\max} = 31.4\ \text{Å}^{-1}$:

$$\begin{aligned} G(r) &= r\left(\frac{1}{2\pi^2 r\rho \sum b^2}\int_{Q_{\min}}^{Q_{\max}} Q[S(Q)-1]\sin(Qr)\mathrm{d}Q\right) \\ &= r(g(r)-1) \end{aligned}$$

where Q is the scattering vector (defined as $Q = 4\pi/\lambda \sin\theta$), λ is the neutron wavelength, θ is the scattering angle, r is real space distance in angstroms, ρ is the experimentally determined sample density, and b is the elemental coherent scattering length of each of the sample's constituent elements. The total correlation function, $T(r)$, was defined as:

$$T(r) = 4\pi r^2 \rho g(r)$$

Small-box structural refinement of the PDFs was performed with the PDFGUI software[30] using the fluorite structure model (ESI Fig. 3†). In total, five parameters were refined: the scale factor, isometric unit cell parameter ($a = b = c$), correlated motion parameter, and the ADPs. The ADPs were isotropic and one ADP parameter was assigned to each Wyckoff site. No refinements resulted in highly correlated parameters.

2.3 X-ray diffraction

Synchrotron X-ray diffraction (XRD) measurements were performed in order to obtain more accurate unit cell parameters and to directly compare the irradiated samples to XRD data from the literature. The XRD samples were prepared according to the procedure outlined by Lang *et al.*[26] The XRD experiments were performed at the High Pressure Collaborative Access Team (HPCAT) 16-BM-D beamline at the Advanced Photon Source (APS) at Argonne National Laboratory using a monochromatic 29.2 keV ($\lambda = 0.4246$ Å) beam. Debye–Scherrer rings were measured in transmission geometry using a Mar345 area detector. The calibration of the detector, the integration of the XRD images, and the determination of the instrument parameters were performed with a CeO_2 NIST standard and GSAS-II.[31] The Rietveld refinements of the integrated diffraction patterns were also performed GSAS-II (ESI Fig. 4†). Unlike the neutron diffractograms, only the scale factor, unit cell parameter, cation ADP, and zero point were refined for the XRD patterns. The oxygen ADP and site occupancy values were taken from the neutron diffraction results, as XRD data do not provide sufficient signal from the anion sublattice to accurately refine these parameters.

3. Results and discussion

The samples were first characterized by inspection of the average structure. The neutron (ESI Fig. 2†) and X-ray (ESI Fig. 4†) diffraction data show that the Bragg diffraction peaks are retained up to the highest fluence achieved (5×10^{12}). Closer inspection reveals that the Bragg peaks shift and undergo subtle broadening at higher ion fluences as a result of increased atomic disorder and the incorporation of heterogeneous microstrain. Plotting the refined unit cell parameters as a function of ion fluence (ESI Fig. 5†) shows that the evolution of volumetric swelling is similar to the trend obtained for CeO_2 and ThO_2 irradiated with 945 MeV Au ions.[32] Despite these similarities, the diffraction measurements do not reveal any information regarding the types of defects that are incorporated because damage accumulation in swift heavy ion (SHI) irradiated CeO_2 and ThO_2 typically proceeds through the production of point defects and does not result in long-range structural modifications, such as phase transformations or amorphization.[22,32–40] In order to better probe the defect structure, the local structure of the material was probed using pair distribution function analysis.

The $T(r)$ functions of CeO_2 and ThO_2 are shown in Fig. 2 for different irradiation fluences. Peaks in the $T(r)$ functions arise from atomic correlations that occur at characteristic distances in real space, r. The position of a correlation represents the mean distance between an interatomic pair with a coordination number that is proportional to the peak area. Notable interatomic pairs from the fluorite structure are labelled. As the ion fluence increases, the intensities of the correlations decrease

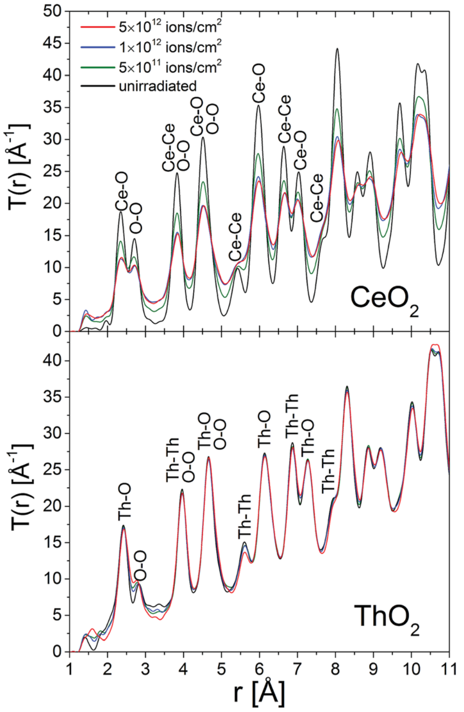

Fig. 2 The total correlation functions, $T(r)$, of CeO_2 (top) and ThO_2 (bottom) for various ion fluences. Notable intra-unit cell correlations are labelled. The legend corresponds to both CeO_2 and ThO_2. As the fluence increases, the intensity of the atomic correlations (peaks) decreases, which signals the loss of coherent scattering intensity from atoms located at ideal sites in the fluorite lattice. The loss of peak intensity as a function of ion fluence is much greater in CeO_2 compared with ThO_2. With the exception of the emergent correlation at $r \sim 1.45$ Å, the loss of coherent scattering intensity and the increase of inter-peak background intensity suggest that irradiation-induced interstitials are distributed over many distinct sites in the structure, *i.e.*, they do not give rise to new atomic correlations.

and intensities in the inter-peak regions generally increase. These changes are much smaller in the case of ThO_2 than for CeO_2. The diminishing peak areas are consistent with a decrease in average coordination numbers and an increase in vacancy concentration.[36] The decrease of peak intensities is not heavily weighted at the high-*r* region, indicating that the materials maintain long-range periodicity, as confirmed by the diffraction data. This suggests that damage accumulation in these materials proceeds *via* point defect accumulation in which atoms are displaced from ideal sites to interstitial positions in the structure. The interstitials are either distributed over many distinct sites in the structure or are too few in concentration, such that the interstitials do not give rise to new atomic correlations in the high-*r* range, *i.e.*, they do not undergo long-range ordering.

These observations are consistent with TEM studies by Takaki *et al.* and Yasuda *et al.*, which note that structural modifications in SHI-irradiated CeO_2 primarily consist of anti-Frenkel pairs and extended defects, such as interstitial-type dislocation loops, line dislocations, and vacancy clusters.[22,33] Looking in detail at the $T(r)$ functions, it is evident that the rate of damage accumulation also differs between the two materials.

The $T(r)$ functions at $\Phi = 1 \times 10^{12}$ and $\Phi = 5 \times 10^{12}$ ions per cm^2 nearly overlap for CeO_2, but not for ThO_2. This suggests that the damage accumulation rate may be slowing in CeO_2 at higher fluences. Indeed, the diffraction data (ESI Fig. 5†) show that the relative change in unit cell parameter for CeO_2 is close to the saturation value of ∼0.06% reported for similar irradiation conditions.[32] This is in contrast to ThO_2 for which the relative change in unit cell parameter is further from the saturation value of ∼0.05% reported for highly energetic ion irradiation.[32] Both materials also show a higher rate of change in unit cell parameter as compared with the results from Tracy *et al.*;[32] however, data from higher fluences, at which saturation of the unit cell expansion is expected to occur, are needed for direct comparison.

Difference curves were constructed in order to better compare and elucidate the evolution of the CeO_2 and ThO_2 PDFs as a function of irradiation fluence. A difference curve is obtained by taking the difference between a PDF and the PDF at the prior fluence (see Fig. 3 caption). The intensity of a difference curve at a given value of *r* corresponds to the change between the two PDFs at that interatomic spacing. These differences arise from peak shifts, changes in peak shape, and changes in peak intensity. The difference curves thus illustrate how the PDF of a material evolves (stepwise) as a function of irradiation fluence. Fig. 3 shows the PDFs of the pristine samples alongside difference curves corresponding to the different irradiation fluences. The amount of local-structure distortion is greater in CeO_2 as compared with ThO_2, which is consistent with the data representation shown in Fig. 2. This confirms that ThO_2 is more structurally stable than CeO_2 under the identical irradiation conditions.

The rate at which local distortions accumulate also differs between the two materials. In CeO_2, the largest distortion occurs at the lowest fluence, $\Phi = 5 \times 10^{11}$ ions per cm^2, with subtler structural modifications occurring at the higher fluences. In ThO_2, the structural disorder accumulates almost linearly as a function of ion fluence. The large initial distortion observed in CeO_2 but not in ThO_2 may be attributed to the introduction of Ce^{3+} through irradiation-assisted redox effects.[32] Cerium has a variable charge state (Ce^{4+}, Ce^{3+}) whereas thorium exhibits a single charge state (Th^{4+}) in the oxide form. The incorporation of Ce^{3+} causes microstrain due to the large size mismatch between Ce^{3+} and Ce^{4+} (1.14 Å and 0.97 Å, respectively[41]). This mechanism provides a means for the rapid accumulation of local distortion in the structure. The redox changes of CeO_2 may also facilitate the formation of more complex defect structures because it provides an additional charge compensation mechanism.

The ThO_2 difference curves show that one of the largest distortions, at any fluence, occurs between $0 < r < 5$ Å, which is centered at around the first nearest neighbor ⟨Th–O⟩ and ⟨O–O⟩ correlations. Based on TEM analysis[22] and molecular dynamics (MD) simulations,[42] the disorder in SHI irradiated fluorite oxides occurs primarily on the anion sublattice. Therefore, it is not surprising that the oxygen correlations exhibit the largest change, as compared with ⟨Th–Th⟩ correlations. The distortion in CeO_2 among the first coordination shells is of lower relative

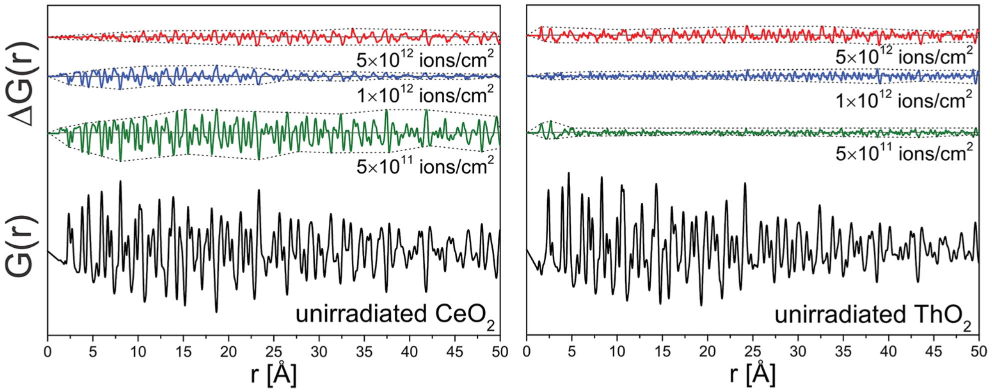

Fig. 3 Pair distribution functions, $G(r)$, of the pristine samples (black) and the difference curves, $\Delta G(r)$, for different fluence steps (colored). $\Delta G(r)$ for fluence 5×10^{11} cm^{-2} is defined as $G(r)$ (5×10^{11}) − $G(r)$ (pristine); $\Delta G(r)$ for fluence 1×10^{12} cm^{-2} is defined as $G(r)$ (1×10^{12}) − $G(r)$ (5×10^{11}), and $\Delta G(r)$ for fluence 5×10^{12} cm^{-2} is defined as: $G(r)$ (5×10^{12}) − $G(r)$ (1×10^{12}). The dotted outlines are guides to the eye. The difference curves demonstrate a large amount of structural distortion of CeO_2 at the lowest fluence, with weaker modifications occurring at the higher fluences. In ThO_2, structural modifications occur at different length scales and are subtler relative to CeO_2.

magnitude compared to those of the higher coordination shells; however, it is unclear whether this variation is an inherent difference in radiation response between CeO_2 and ThO_2 or an artifact of the difference curve construct. Difference curves are influenced by both unit cell expansion (peak shifts) and local structure disordering (changes in peak shape and relative intensity). Thus, the high-*r* intensities and lack of low-*r* intensity observed for CeO_2 can be attributed to either greater swelling, more complex defect clusters, and/or larger defect concentrations. It is difficult to ascribe the cause from the difference curves alone because the peaks shifts are more heavily weighted at the higher-*r* region.

In order to circumvent this problem, the PDFs were refined using the boxcar method. Boxcar fitting is a technique by which small bins of *r*-space are individually refined to reveal distortions that might otherwise be undetected in full-profile refinements.[43] The PDFs were binned into five 10 Å ranges that were individually refined with a fluorite structural model. This enabled the separation of the unit cell expansion from defect disordering contributions to the PDF modifications. As a result, discrepancies between the $Fm\bar{3}m$ model and the fitted PDF arise only from atomic disordering and not changes in the unit cell parameter.

The discrepancies between the fluorite-structure model and fitted PDFs were quantified by the fit agreement factor, R_w:

$$R_w = \sqrt{\frac{\sum_{i=1}^{n} \omega(r_i)\left[G_{obs}(r_i) - G_{calc}(r_i)\right]^2}{\sum_{i=1}^{n} \omega(r_i) G_{obs}{}^2(r_i)}}$$

where G_{obs} is the measured PDF, G_{calc} is the fitted PDF, and ω is a weighting factor. This approach allows the determination of the spatial distribution of disorder. Fig. 4 shows the relative change in R_w of the irradiated samples, normalized to the R_w values of the unirradiated samples, as a function of *r*-space bin position. The results show that disorder accumulates primarily in the low-*r* region (*i.e.*, the short-range structure) of CeO_2 at intermediate fluences. Upon reaching the highest fluence, the disorder is accrued equally throughout the *r* range. ThO_2 exhibits a different trend in which disorder accumulates primarily in the higher-*r* bins (*i.e.*, the intermediate-range structure). In contrast to CeO_2, the discrepancy in ΔR_w between the low- and high-*r* regions increases as a function of fluence for ThO_2.

The small improvement in the fit in the low-*r* region may be attributed to the recovery or rearrangement of intrinsic defects in the starting material, such as oxygen defects[44] and F-centers[45] that have been observed in unirradiated ThO_2 single crystals. The preferential accumulation of distortion at high-*r* can be explained by changes in the domain size, which is representative of the average crystallite size. Inspection of the PDFs shows that the intensity of the PDF at high-*r* decreases as the fluence increases. This, coupled with the information from Fig. 4, indicates that ThO_2 undergoes a slight decrease in

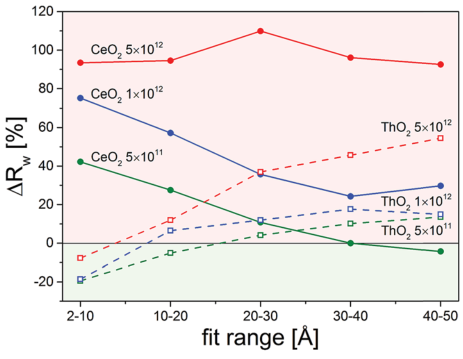

Fig. 4 Relative change of the goodness-of-fit parameter, ΔR_w, as a function of binned *r*-space range for fitting of the $Fm\bar{3}m$ structure to the pair distribution functions. The data are normalized to the R_w values of the pristine samples, as represented by the $\Delta R_w = 0$ baseline. Negative ΔR_w values represent an improvement in the fit (green shaded area) and positive ΔR_w values represent a worsening of the fit (red shaded area). As the fluence increases, the short-range structure (low *r*) and the intermediate-range structure (higher *r*) exhibit the largest distortion in CeO_2 and ThO_2, respectively.

domain (crystallite) size after irradiation. Similar behavior is observed for CeO_2; however, the changes in domain size (high-*r*) are dwarfed by changes in the short range structure (low-*r*) at intermediate fluences. Swift heavy ion irradiation-induced polygonization of CeO_2 crystallites into smaller sub-grains has been observed by TEM and is attributed to the formation of dislocation networks following the accumulation and agglomeration of interstitials.[33] Similar behavior has been reported in fluorite-structured UO_2 and yttria-stabilized zirconia, suggesting that it is a general response of oxides with this structure.[46,47]

The stark difference in defect accumulation behavior between CeO_2 and ThO_2 suggests that the two materials accommodate defects very differently. To this end, inspection of the short-range structure provides further insight. Fig. 5 and ESI Table 1† show that the first nearest neighbor (1-NN) cation–oxygen and cation–cation spacings in both materials increase after irradiation to 5×10^{12} ions per cm^2. The ⟨Ce–O⟩ peak broadens symmetrically whereas the ⟨Th–O⟩ peak broadens asymmetrically at higher *r*. Likewise, the ⟨O–O⟩ peaks also show different behavior. In CeO_2, the ⟨Ce–O⟩ and ⟨O–O⟩ distances both decrease before eventually increasing after the highest fluence. In ThO_2, the ⟨O–O⟩ peak shows an overall shift to lower *r*. These changes provide clues as to how defects, specifically vacancies, are incorporated into the two oxides.

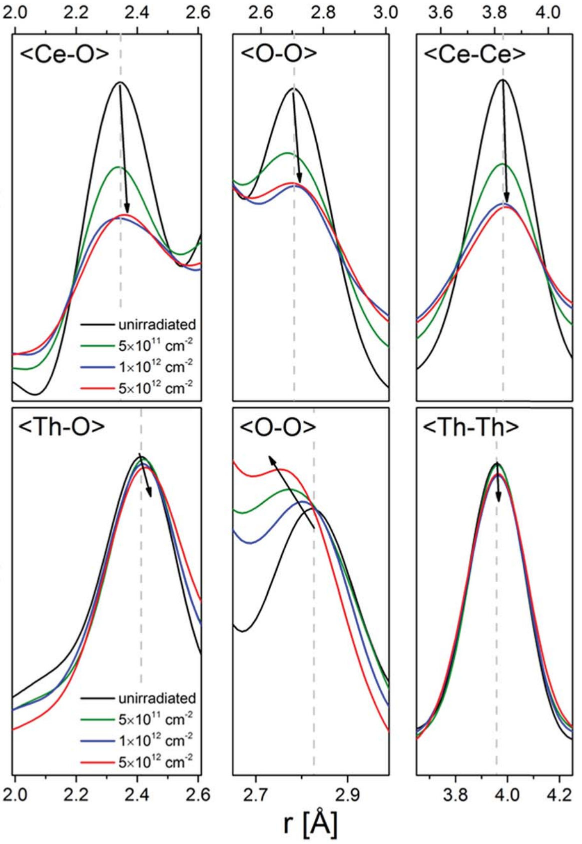

Fig. 5 PDF peak evolution of the first nearest-neighbor (1-NN) cation–oxygen, oxygen–oxygen, and cation–cation correlations for various ion fluences. Black arrows indicate the overall trend for the peak shift with increasing fluence.

In CeO_2, the incorporation of an oxygen vacancy involves the removal of the attractive interaction between a cation and one of its eight surrounding anions. This promotes the relaxation of the remaining nearest-neighbor oxygens towards the central cation and results in the shortening of the mean cation–oxygen distance. More recently, Muhich[48] has shown that the contractions of the ⟨Ce–O⟩ distance can be explained by considering non-counterpoised forces. By similar argument, it can be shown that the mean ⟨O–O⟩ distance should also increase. The relaxation of 1-NN oxygens surrounding an oxygen vacancy is larger than the relaxation of second nearest-neighbor (2-NN) oxygens. The ⟨O–O⟩ distance among the 1-NNs decreases whereas the ⟨O–O⟩ distance between the 1-NNs and 2-NNs increases. The 2-NN oxygens outnumber the 1-NN oxygens 2 : 1; therefore, the result is an overall increase in the ⟨O–O⟩ distance. This behavior has been reported for CeO_2 doped with trivalent lanthanides to produce vacancies by charge equilibrium effects.[49,50] The increase of the 1-NN ⟨Ce–Ce⟩ distance is consistent with the incorporation of Ce^{3+} and unit cell expansion, which results from defect accumulation.

Moreover, it has also been shown[32,34] that dense electronic excitation from ion irradiation can result in the reduction of cerium atoms, although the relative concentration of Ce^{3+} is expected to be low.[51] The steady incorporation of Ce^{3+} into the CeO_2 structure increases the mean ⟨Ce–O⟩ distance because ⟨Ce^{3+}–O⟩ distances are larger than ⟨Ce^{4+}–O⟩ distances on account of decreased Coulomb interactions and the increased ionic radius of Ce^{3+} compared to Ce^{4+}.[52] This may explain why the ⟨Ce–O⟩ peak broadens at the intermediate fluences and eventually shifts to higher *r* at the highest fluence, *i.e.*, the effects of redox-driven disorder are larger at the higher ion fluences. Rietveld analysis suggests a more gradual increase in cerium reduction with increasing ion fluence. The oxygen content at the 8*c* site determined from analysis of the neutron diffraction patterns shows a steady decrease with increasing ion fluence: occupancy = 1.0000, 0.9954, 0.9925, and 0.9914, corresponding to $x = 0$, 0.009, 0.015, 0.017 in CeO_{2-x} for unirradiated, 5×10^{11}, 1×10^{12}, and 5×10^{12} samples, respectively. However, the 8*c* site occupancy alone may not be sufficient to quantify the amount of reduction owing to the very heterogeneous defect structure that is formed in ion irradiated CeO_2.

Takaki *et al.*[22] showed that ion tracks in CeO_2 consist of an oxygen-deficient core region and an oxygen-rich halo region. Within these two regions, and especially at the interface between these regions, the behavior of first nearest-neighbor atom distances is not easily predicted. As described in other studies,[48,53] the reduction of ceria leads to competing effects of lattice contraction and expansion on different length scales. Simple models may not be easily applied to understand ion irradiated CeO_2 because of the defect concentration gradients associated with irradiation-induced atomic displacement. The use of spectroscopy techniques, such as in-track electron energy-loss spectroscopy (EELS),[16] are necessary to more accurately assess the spatial extent of reduction in irradiated CeO_2.

Regarding ThO_2, the PDFs show that the ⟨Th–O⟩ peak broadens asymmetrically and shifts to higher *r*. The asymmetric shift to higher *r* is unexpected because it suggests that ThO_2

may exhibit non-ionic character contrary to the behavior of CeO_2 described above, *i.e.*, the atom relaxation behavior cannot be explained by assuming fully ionic defects. A deviation from ionic character is unexpected considering that ThO_2 exhibits less covalency as compared with CeO_2.[54] One possible explanation for the unexpected peak evolution is that irradiated ThO_2 has mostly charged defects. The preferential accumulation of charged vacancies, for example, may alter the process of atom relaxation. The production of charged defects can be rationalized as a charge compensation requirement considering that thorium presumably has a high 5th ionization energy owing to the lack of non-stoichiometry in air in the Th–O phase diagram.[55] Positively charged vacancies are predicted to exist in hypostoichiometric ThO_2,[56] and F-centers have been observed in single crystal ThO_2.[57] Of these examples, positively charged vacancies are noteworthy because it has been proposed that swift heavy ion irradiation of ThO_2 may result in the formation of local, non-stoichiometric regions.[40] Thus, the formation of local regions of hypo- and hyper-stoichiometry within a nominally stoichiometric ThO_2 sample provides a mechanism for the formation of charged defects. This would explain the divergent behavior of ThO_2 and CeO_2 with respect to cation coordination distance due to irradiation, as oxidation state changes of Ce provide an alternate means of charge compensation not accessible to Th.

Alternatively, the unique peak evolution in the PDFs of ThO_2 can be explained by a distortion of local polyhedra. The minimal change in the $\langle$Th–O$\rangle$ and $\langle$Th–Th$\rangle$ correlations, in conjunction with the highly modified $\langle$O–O$\rangle$ correlation, suggests that a largely undistorted cation sublattice coexists with a relatively-distorted oxygen sublattice. The large decrease in the $\langle$O–O$\rangle$ distance and the relatively small change in the $\langle$Th–O$\rangle$ distance are indicative of a decrease in the mean O–Th–O bond angle. This change can result from the replacement of cubic ThO_8 units by distorted ThO_8 units in the simple cubic oxygen sublattice that are caused by defects and/or irradiation-induced changes in bonding.

Finally, signatures of short-range interstitial species were identified by examining atomic correlations at low r. For CeO_2, inspection of the low r region in Fig. 2 reveals the emergence of a small peak at around $r \sim 1.45$ Å following irradiation. The $T(r)$ functions of ThO_2 exhibit a similar feature after irradiation; however, the PDFs of the ThO_2 samples exhibited more noise compared with the CeO_2 samples, which makes the interpretation of the new peak speculative. The correlation at $r \sim 1.45$ Å in CeO_2 bears a striking resemblance to a peak observed in an *ab initio* MD investigation by Xiao *et al.*[58] of electronically excited titanate pyrochlores, which are ternary f-block element-bearing oxides with fluorite-derived structures. Xiao *et al.*[58] attributed this correlation to an O_2-like defect that forms after irradiation; however, the correlation in the present study can be attributed to oxygen dimer and/or peroxide defects.[59]

The peroxide ion is a bound state of two oxygen interstitials with a $\langle$O–O$\rangle$ bond length of ~1.49 Å and an overall charge state of −2.[60] The $\langle$O–O$\rangle$ spacing of peroxide more closely matches the observed correlation position at $r \sim 1.45$ Å than does the bond length of ~1.24 Å exhibited by charge-neutral O_2 molecules. The presence of other interstitial dimer configurations is also possible,[35] although the $\langle$O–O$\rangle$ distance of these defects typically ranges from ~1.35–1.45 Å depending on the material and charge state of the defect.[61] The presence of peroxide is also conceivable when considering cation redox. Unlike UO_2, the cations of CeO_2 and ThO_2 cannot easily oxidize to accommodate excess negative charge from oxygen interstitials. Cerium typically reduces to the Ce^{3+} state whereas thorium is typically fixed in the 4+ state as an oxide. Peroxide molecules are unique from split di-interstitials and O_2 molecules in that they exhibit a charge state identical to anions ($[O–O]^{2-}$ compared to O^{2-}) and cause minimal displacement of nearby atoms.[59] Thus, peroxide ions can be accommodated more easily in the structure without the need for further charge compensation mechanisms, such as cation oxidation.

Analogous to the case of UO_{2+x}, in which oxygen defect cluster formation is established as a dynamic competition between repulsive Coulomb- and attractive orbital hybridization effects,[62] the large difference in the local structural distortion between CeO_2 and ThO_2 indirectly illustrates the influence of electronic structure on the radiation response under swift heavy ion irradiation. The local structural distortions observed in CeO_2 are largely explained by the incorporation of vacancies whereas the disorder in ThO_2 appears more driven by the incorporation of interstitials. In both cases, interstitial formation is accommodated by efficient interstitial agglomeration, as indicated by the presence of peroxide in CeO_2 and domain-size reduction in ThO_2. The observation of peroxide in CeO_2 supports the notion that displaced oxygen interstitials are largely bound and remain in the system instead of leaving grains *via* diffusion to grain boundaries and/or O_2 molecule formation.[61] Peroxide formation is not only an efficient mechanism for incorporating excess oxygen in these systems, but it may also promote further reduction if, under certain conditions, the formation of peroxide or superoxide ($O_2{}^{-}$) frees electrons to localize on the 4*f* band of nearby cerium atoms.

The identification and attribution of the small $\langle$O–O$\rangle$ correlations in the CeO_2 PDFs to peroxide is also notable because recent studies have predicted the formation of peroxide defects in a variety of oxide systems, such as perovskites,[63] CeO_2,[59] and nuclear fuel materials, such as ThO_2 (ref. 56 and 59) and UO_2.[64–67] In the latter system it has been shown that certain oxygen defect clusters exhibit fast diffusion pathways[68,69] that directly influence predictions of bulk transport properties when incorporated in multi-scale engineering models.[70] Therefore, it is conceivable that similar concepts may apply to other fluorite structure systems, especially when considering that the migration energies for peroxide defects (0.79 and 0.89 eV in CeO_2 and ThO_2, respectively[59]) are comparable to the calculated migration energies of O^{2-} interstitials (0.80 and 1.04 eV in CeO_2 and ThO_2, respectively[61]). Obtaining a better understanding of the role of peroxide and analogous defects in bulk transport in CeO_2 systems will enable more accurate prediction of properties and design of fast ion conductor materials.

4. Conclusions

Defect accumulation mechanisms in swift heavy ion irradiated CeO_2 and ThO_2 were investigated using pair distribution function analysis (PDF) of neutron total scattering measurements. The total correlation functions, $T(r)$, PDF difference curves, and small-box refinement results demonstrated that CeO_2 exhibits more disordering than ThO_2 under identical irradiation conditions. A comparison of the shifts of the first nearest-neighbor cation–oxygen, oxygen–oxygen, and cation–cation correlations showed that the response of the local structure is different between isostructural CeO_2 and ThO_2, even if similar defects are formed. The distortion of the local structure of CeO_2 appears to be driven by the accumulation of vacancies. The $T(r)$ functions revealed that a small correlation appears at $r \sim 1.45$ Å in CeO_2 after irradiation. This new correlation was attributed to the formation of peroxide and/or oxygen dimers. In contrast to CeO_2, the structural distortion of ThO_2 may be driven by the formation of charged defects or larger defect aggregates. A change in the mean O–Th–O angle with fluence suggests that irradiation results in the distortion of local ThO_8 polyhedra.

Acknowledgements

This research is funded by the Office of Basic Energy Sciences of the U.S. Department of Energy as part of the Materials Science of Actinides Energy Frontier Research Center (DE-SC0001089). The research at ORNL's Spallation Neutron Source was sponsored by the Scientific User Facilities Division, Office of Basic Energy Sciences, US Department of Energy. A portion of this work was performed at HPCAT (Sector 16), Advanced Photon Source (APS), Argonne National Laboratory. HPCAT operations are supported by DOE-NNSA under Award No. DE-NA0001974 and DOE-BES under Award No. De-FG02-99ER45775, with partial instrumentation funding by NSF. This research used resources at the Advanced Photon Source, a U.S. Department of Energy (DOE) Office of Science User Facility operated for the DOE Office of Science by Argonne National Laboratory under Contract No. De-AC02-06CH11357. HPCAT beamtime was granted by the Carnegie/DOE Alliance Center (CDAC). R.I.P. gratefully acknowledges support from the U.S. Department of Energy (DOE) National Nuclear Security Administration (NNSA) through the Carnegie DOE Alliance Center (CDAC) under grant number DE-NA-0002006.

References

1 A. Trovarelli, C. de Leitenburg, M. Boaro and G. Dolcetti, *Catal. Today*, 1999, **50**, 353–367.
2 T. Tabakova, V. Idakiev, K. Tenchev, F. Boccuzzi, M. Manzoli and A. Chiorino, *Appl. Catal., B*, 2006, **63**, 94–103.
3 H. J. Beie and A. Gnörich, *Sens. Actuators, B*, 1991, **4**, 393–399.
4 IAEA, *Thorium Fuel Cycle – Potential Benefits and Challenges TECDOC-1450, Report 1011–4289*, Vienna, Austria, 2005.
5 M. Lung and O. Gremm, *Nucl. Eng. Des.*, 1998, **180**, 133–146.
6 J. S. Herring, P. E. MacDonald, K. D. Weaver and C. Kullberg, *Nucl. Eng. Des.*, 2001, **203**, 65–85.
7 J. B. Goodenough, *Annu. Rev. Mater. Res.*, 2003, **33**, 91–128.
8 H. L. Tuller, *Solid State Ionics*, 1992, **52**, 135–146.
9 D. A. Andersson, S. I. Simak, N. V. Skorodumova, I. A. Abrikosov and B. Johansson, *Proc. Natl. Acad. Sci. U. S. A.*, 2006, **103**, 3518–3521.
10 M. Li, M. J. Pietrowski, R. A. De Souza, H. Zhang, I. M. Reaney, S. N. Cook, J. A. Kilner and D. C. Sinclair, *Nat. Mater.*, 2014, **13**, 31–35.
11 P. Lacorre, F. Goutenoire, O. Bohnke, R. Retoux and Y. Laligant, *Nature*, 2000, **404**, 856–858.
12 Y. Lin, S. Fang, D. Su, K. S. Brinkman and F. Chen, *Nat. Commun.*, 2015, **6**, 6824.
13 D. S. Aidhy, B. Liu, Y. Zhang and W. J. Weber, *J. Phys. Chem. C*, 2014, **118**, 30139–30144.
14 D. S. Aidhy, R. Sachan, E. Zarkadoula, O. Pakarinen, M. F. Chisholm, Y. Zhang and W. J. Weber, *Sci. Rep.*, 2015, **5**, 16297.
15 J. Lian, L. M. Wang, S. X. Wang, J. Chen, L. A. Boatner and R. C. Ewing, *Phys. Rev. Lett.*, 2001, **87**, 145901.
16 R. Sachan, V. R. Cooper, B. Liu, D. S. Aidhy, B. K. Voas, M. Lang, X. Ou, C. Trautmann, Y. Zhang, M. F. Chisholm and W. J. Weber, *J. Phys. Chem. C*, 2017, **121**, 975–981.
17 D. M. Duffy, S. L. Daraszewicz and J. Mulroue, *Nucl. Instrum. Methods Phys. Res., Sect. B*, 2012, **277**, 21–27.
18 N. Itoh, D. M. Duffy, S. Khakshouri and A. M. Stoneham, *J. Phys.: Condens. Matter*, 2009, **21**, 474205.
19 P. Kluth, C. S. Schnohr, O. H. Pakarinen, F. Djurabekova, D. J. Sprouster, R. Giulian, M. C. Ridgway, A. P. Byrne, C. Trautmann, D. J. Cookson, K. Nordlund and M. Toulemonde, *Phys. Rev. Lett.*, 2008, **101**, 175503.
20 C. L. Tracy, M. Lang, F. Zhang, C. Trautmann and R. C. Ewing, *Phys. Rev. B: Condens. Matter Mater. Phys.*, 2015, **92**, 174101.
21 B. Afra, M. D. Rodriguez, C. Trautmann, O. H. Pakarinen, F. Djurabekova, K. Nordlund, T. Bierschenk, R. Giulian, M. C. Ridgway, G. Rizza, N. Kirby, M. Toulemonde and P. Kluth, *J. Phys.: Condens. Matter*, 2013, **25**, 045006.
22 S. Takaki, K. Yasuda, T. Yamamoto, S. Matsumura and N. Ishikawa, *Nucl. Instrum. Methods Phys. Res., Sect. B*, 2014, **326**, 140–144.
23 IAEA, *Viability of inert matrix fuel in reducing plutonium amounts in reactors TECDOC-1516*, Vienna, Austria, 2006.
24 C. Lombardi, L. Luzzi, E. Padovani and F. Vettraino, *Prog. Nucl. Energy*, 2008, **50**, 944–953.
25 J. F. Ziegler, M. D. Ziegler and J. P. Biersack, *Nucl. Instrum. Methods Phys. Res., Sect. B*, 2010, **268**, 1818–1823.
26 M. Lang, F. X. Zhang, J. M. Zhang, C. L. Tracy, A. B. Cusick, J. VonEhr, Z. G. Chen, C. Trautmann and R. C. Ewing, *Nucl. Instrum. Methods Phys. Res., Sect. B*, 2014, **326**, 121–125.
27 E. Luther, C. Necker, B. Mihaila, P. Papin and D. Guidry, *Trans. Am. Nucl. Soc.*, 2011, **104**, 257–258.
28 J. Neuefeind, M. Feygenson, J. Carruth, R. Hoffmann and K. K. Chipley, *Nucl. Instrum. Methods Phys. Res., Sect. B*, 2012, **287**, 68–75.
29 B. Toby, *J. Appl. Crystallogr.*, 2001, **34**, 210–213.

30 C. L. Farrow, P. Juhas, J. W. Liu, D. Bryndin, E. S. Bozin, J. Bloch, T. Proffen and S. J. L. Billinge, *J. Phys.: Condens. Matter*, 2007, **19**, 335219.

31 B. H. Toby and R. B. Von Dreele, *J. Appl. Crystallogr.*, 2013, **46**, 544–549.

32 C. L. Tracy, M. Lang, J. M. Pray, F. Zhang, D. Popov, C. Park, C. Trautmann, M. Bender, D. Severin, V. A. Skuratov and R. C. Ewing, *Nat. Commun.*, 2015, **6**, 6133.

33 K. Yasuda, M. Etoh, K. Sawada, T. Yamamoto, K. Yasunaga, S. Matsumura and N. Ishikawa, *Nucl. Instrum. Methods Phys. Res., Sect. B*, 2013, **314**, 185–190.

34 A. Iwase, H. Ohno, N. Ishikawa, Y. Baba, N. Hirao, T. Sonoda and M. Kinoshita, *Nucl. Instrum. Methods Phys. Res., Sect. B*, 2009, **267**, 969–972.

35 M. Iwasawa, T. Ohnuma, Y. Chen, Y. Kaneta, H. Y. Geng, A. Iwase and M. Kinoshita, *J. Nucl. Mater.*, 2009, **393**, 321–327.

36 H. Ohno, A. Iwase, D. Matsumura, Y. Nishihata, J. Mizuki, N. Ishikawa, Y. Baba, N. Hirao, T. Sonoda and M. Kinoshita, *Nucl. Instrum. Methods Phys. Res., Sect. B*, 2008, **266**, 3013–3017.

37 N. Ishikawa, Y. Chimi, O. Michikami, Y. Ohta, K. Ohhara, M. Lang and R. Neumann, *Nucl. Instrum. Methods Phys. Res., Sect. B*, 2008, **266**, 3033–3036.

38 T. Sonoda, A. Kinoshita, N. Ishikawa, M. Sataka, Y. Chimi, N. Okubo, A. Iwase and K. Yasunaga, *Nucl. Instrum. Methods Phys. Res., Sect. B*, 2008, **266**, 2882–2886.

39 T. Sonoda, M. Kinoshita, Y. Chimi, N. Ishikawa, M. Sataka and A. Iwase, *Nucl. Instrum. Methods Phys. Res., Sect. B*, 2006, **250**, 254–258.

40 C. L. Tracy, J. M. Pray, M. Lang, D. Popov, C. Park, C. Trautmann and R. C. Ewing, *Nucl. Instrum. Methods Phys. Res., Sect. B*, 2014, **326**, 169–173.

41 R. D. Shannon, *Acta Crystallogr., Sect. A: Cryst. Phys., Diffr., Theor. Gen. Crystallogr.*, 1976, **32**, 751–767.

42 D. S. Aidhy, D. Wolf and A. El-Azab, *Scr. Mater.*, 2011, **65**, 867–870.

43 X. Qiu, T. Proffen, J. F. Mitchell and S. J. L. Billinge, *Phys. Rev. Lett.*, 2005, **94**, 177203.

44 T. D. Kelly, J. C. Petrosky, J. W. McClory, J. M. Mann and J. W. Kolis, *Phys. Status Solidi RRL*, 2015, **9**(11), 668–672.

45 B. G. Childs, P. J. Harvey and J. B. Hallett, *J. Am. Ceram. Soc.*, 1970, **53**, 431–435.

46 F. Garrido, S. Moll, G. Sattonnay, L. Thomé and L. Vincent, *Nucl. Instrum. Methods Phys. Res., Sect. B*, 2009, **267**, 1451–1455.

47 K. E. Sickafus, H. Matzke, K. Yasuda, I. I. I. P. Chodak, R. A. Verrall, P. G. Lucuta, H. R. Andrews, A. Turos, R. Fromknecht and N. P. Baker, *Nucl. Instrum. Methods Phys. Res., Sect. B*, 1998, **141**, 358–365.

48 C. L. Muhich, *J. Phys. Chem. C*, 2017, **121**, 8052–8059.

49 M. Coduri, M. Scavini, M. Brunelli and P. Masala, *Phys. Chem. Chem. Phys.*, 2013, **15**, 8495–8505.

50 H. Hayashi, R. Sagawa, H. Inaba and K. Kawamura, *Solid State Ionics*, 2000, **131**, 281–290.

51 C. A. Yablinsky, R. Devanathan, J. Pakarinen, J. Gan, D. Severin, C. Trautmann and T. R. Allen, *J. Mater. Res.*, 2015, **30**, 1473–1484.

52 Z. Cui, Y. Sun and J. Qu, *Solid State Ionics*, 2012, **226**, 24–29.

53 D. Marrocchelli, S. R. Bishop, H. L. Tuller and B. Yildiz, *Adv. Funct. Mater.*, 2012, **22**, 1958–1965.

54 H. Y. Xiao and W. J. Weber, *J. Phys. Chem. B*, 2011, **115**, 6524–6533.

55 C. Keller, in *Comprehensive Inorganic Chemistry*, ed. H. J. EmelÉUs, R. Nyholm and A. F. Trotman-Dickenson, Pergamon, Oxford, 1973, pp. 219–276, DOI: 10.1016/B978-1-4832-8313-5.50027-9.

56 S. T. Murphy, M. W. D. Cooper and R. W. Grimes, *Solid State Ionics*, 2014, **267**, 80–87.

57 V. I. Neeley, J. B. Gruber and W. J. Gray, *Phys. Rev.*, 1967, **158**, 809–813.

58 H. Y. Xiao, W. J. Weber, Y. Zhang, X. T. Zu and S. Li, *Sci. Rep.*, 2015, **5**, 8265.

59 S. C. Middleburgh, G. R. Lumpkin and R. W. Grimes, *Solid State Ionics*, 2013, **253**, 119–122.

60 S. C. Abrahams and J. Kalnajs, *Acta Crystallogr.*, 1954, **7**, 838–842.

61 H. Y. Xiao, Y. Zhang and W. J. Weber, *Acta Mater.*, 2013, **61**, 7639–7645.

62 D. A. Andersson, J. Lezama, B. P. Uberuaga, C. Deo and S. D. Conradson, *Phys. Rev. B: Condens. Matter Mater. Phys.*, 2009, **79**, 024110.

63 S. C. Middleburgh, I. Karatchevtseva, B. J. Kennedy, P. A. Burr, Z. Zhang, E. Reynolds, R. W. Grimes and G. R. Lumpkin, *J. Mater. Chem. A*, 2014, **2**, 15883–15888.

64 N. A. Brincat, M. Molinari, S. C. Parker, G. C. Allen and M. T. Storr, *J. Nucl. Mater.*, 2015, **456**, 329–333.

65 N. A. Brincat, M. Molinari, G. C. Allen, M. T. Storr and S. C. Parker, *J. Nucl. Mater.*, 2015, **467**, 724–729.

66 D. A. Andersson, G. Baldinozzi, L. Desgranges, D. R. Conradson and S. D. Conradson, *Inorg. Chem.*, 2013, **52**, 2769–2778.

67 J. W. Wang, R. C. Ewing and U. Becker, *Phys. Rev. B: Condens. Matter Mater. Phys.*, 2013, **88**, 024109.

68 D. A. Andersson, T. Watanabe, C. Deo and B. P. Uberuaga, *Phys. Rev. B: Condens. Matter Mater. Phys.*, 2009, **80**, 060101(R).

69 J. Wang, R. C. Ewing and U. Becker, *Sci. Rep.*, 2014, **4**, 4216.

70 M. Bertolus, M. Freyss, B. Dorado, G. Martin, K. Hoang, S. Maillard, R. Skorek, P. Garcia, C. Valot, A. Chartier, L. Van Brutzel, P. Fossati, R. W. Grimes, D. C. Parfitt, C. L. Bishop, S. T. Murphy, M. J. D. Rushton, D. Staicu, E. Yakub, S. Nichenko, M. Krack, F. Devynck, R. Ngayam-Happy, K. Govers, C. S. Deo and R. K. Behera, *J. Nucl. Mater.*, 2015, **462**, 475–495.